Astronomy & Astrophysics manuscript no. output
July 6, 2026

The twist of solar magnetic-flux ropes

I. Method for twist estimation and statistical analysis

B. D. Dorsch[1,2,⋆], J. Magdalenić[1,2], and L. Rodriguez[1]

[1] Solar-Terrestrial Centre of Excellence – SIDC, Royal Observatory of Belgium, Ringlaan -3- Av. Circulaire, 1180 Brussels, Belgium
[2] KU Leuven, Centre for mathematical Plasma Astrophysics Celestijnenlaan 200B, Leuven

Received September 30, 20XX

ABSTRACT

Context. Magnetic flux ropes (MFRs) are ubiquitous structures observed in the solar corona and one of the main components of coronal mass ejections (CMEs). A key input parameter for advanced heliospheric magnetohydrodynamic models of CME propagation is the twist, which quantifies the rotation of magnetic field lines around their axis. As CMEs are the drivers of the strongest geomagnetic storms, their accurate modelling, including twist estimation, has a large impact on space weather (SW).

Aims. The estimation of MFR twist requires time-consuming processes and/or high-quality cadence data, which presents constraints for the SW forecasting workflow. We developed a method to estimate the twist that is easily integrated in SW operations. The method is tested in a comprehensive statistical analysis.

Methods. The twist is estimated by the ratio of axial length and minor radius of the MFR from a selected extreme-ultraviolet (EUV) image. We applied the method, for which we developed a tool, and estimated the twist of 43 MFR events observed simultaneously in EUV data by one or more spacecraft. Each MFR is associated with a CME and the majority with flaring activity.

Results. We found a clear and consistent dependence of the estimated twist on the viewpoint. We observe a systematic decrease of the twist value when the MFR structure is seen closer to the solar limb. We thus derive a regression model to estimate the twist at a desired longitude. In addition, our work revealed a strong correlation between the twist of a MFR and the CME speed, in particular for events associated with low to moderate flare energies. This has a strong influence on the simulation of the propagation of magnetised CMEs. We provide an empirical relation that offers a diagnostic proxy of the twist for post-event analyses and real-time SW forecasting framework.

Key words. twist – FRi3D – coronal mass ejections

1. Introduction

Two of the most energetic dynamic processes on the Sun, which often appear synchronously in space and time, are solar flares and coronal mass ejections (CMEs). Solar flares are large releases of energy across the full wavelength spectrum (see e.g. Gold & Hoyle 1960). CMEs are large-scale eruptions of plasma and magnetic field from the Sun to the heliosphere. They are one of the main drivers of space weather (SW) and the source of the strongest geomagnetic storms at Earth. In white-light observations, CMEs often show a three-part structure: core, cavity, and a leading edge (Section 4). CME eruptions are associated with the release of large amounts of energy accumulated in the low corona, with different possible triggering mechanisms (see e.g. Temmer 2021). The magnetic energy is the only source in the corona large enough to produce them, as the gravitational, thermal, and kinetic energies fall below the required thresholds (Forbes 2000). Therefore, it is important to understand how much magnetic energy is accumulated in the corona prior to a CME eruption. Multiwavelength observations suggest that energy is stored in the highly sheared and/or twisted magnetic fields (van Ballegooijen et al. 2007) located in the active regions (ARs) and low corona. These complex magnetic structures, which we refer to as magnetic flux ropes (MFRs), are an intrinsic part of a CME (Priest & Longcope 2017). MFRs are coherent structures composed of helical magnetic-field lines that wind around a common axis, forming a toroidal configuration generated by a central current channel and its self-induced magnetic field (Chen 2017). The twisted magnetic-field-line topology of a MFR is indicative of available free energy and magnetic helicity stored within these magnetic structures (Chintzoglou et al. 2015). The magnetic helicity describes the geometrical complexity of magnetic-field lines through the twist and writhe (Moffatt 1978; Berger 1999), which are fundamental properties of a MFR and key to understanding the evolution of CMEs (Berger & Ruzmaikin 2000; Priest et al. 2016).

Predicting the arrival time and geo-effectiveness of CMEs was the focus of the majority of the space-weather-related studies of the last several decades. One of the state-of-the-art solar-wind and CME modelling tools, which was also employed in this study, is the 3D magnetohydrodynamic (MHD) model EUHFORIA (The EUropean Heliospheric FORecasting Information Asset, Pomoell & Poedts 2018). One of the three main parts of this space-weather inner heliosphere model is the CME insertion part, which starts at 0.1 au—i.e. the inner boundary of the model. Various CME models can be incorporated within EUHFORIA. The cone model (see e.g. Xie et al. 2004) is one of the most widely used models due to its simplicity and rather accurate prediction of the ICME (interplanetary CME) arrival time at Earth (Rodriguez et al. 2024). Nevertheless, the unmagnetised conical representation of the CME fails to provide a

⋆ Corresponding author: brenda.dorsch@observatory.be

Article published by EDP Sciences, to be cited as https://doi.org/10.1051/0004-6361/202659412

physical description of the CME magnetic structure. The most advanced models used to characterise the evolution of a CME and its space-weather impact include a magnetic description of the CME structure. FRi3D (Flux Rope in 3D, Isavnin 2016) is a state-of-the-art 3D CME model capable of reproducing its global geometrical shape and its 3D magnetic-field structure more accurately than other CME models, for example spheromak (see e.g. Verbeke et al. 2019; Asvestari et al. 2021). The geometry of FRi3D consists of a cylindrical shell with an axis described as a non-circular changing curve and a radius that is variable along the axis. The deformations in the geometry are captured by a number of free parameters defined as pancaking, flattening, and skew (Maharana et al. 2022). Although similar to a torus shape, the geometry of FRi3D offers more flexibility; hence, it better approximates features commonly interpreted as flux rope legs and thus also allows us to more accurately simulate flank encounters. The CME magnetic properties inserted in FRi3D are the polarity and chirality of the magnetic structure, the total magnetic flux associated with the eruption, and the twist of the flux rope.

Defining the input parameters is an initial and important step in CME modelling. The parameters that describe the geometry, the direction of propagation, and the speed of the CME are routinely derived from observations (e.g. Scolini et al. 2019; Palmerio et al. 2017). The magnetic-flux estimation requires a higher level of data processing, and there is no established consensus on the most appropriate methodology for its estimation. The temperature and density of the CME are difficult to estimate, and generally an average value is used (Scolini et al. 2020). The twist of the MFR is also a complex parameter to estimate, and a fixed value is currently used in FRi3D.

The magnetic twist can be estimated using different methods, but most of them are not easily integrated into time-sensitive space-weather-forecasting workflows, since they involve time-consuming analysis and/or require high-quality vector magnetic data. We briefly list some of the most often used methods, starting with non-linear force-free field (NLFFF) extrapolations, in which the three-dimensional coronal magnetic field is reconstructed from a vector magnetogram and the field-line twist is computed (Wiegelmann 2004; Guo et al. 2010; Inoue et al. 2013). At the photospheric level, the force-free parameter α, derived from vertical current density and magnetic-field components, serves as a proxy for magnetic twist and non-potentiality (Seehafer 1990; Murray, M. J. & Hood, A. W. 2008). Analytical flux-rope models, such as the Titov–Démoulin configuration, are often fitted to coronal structures such as filaments and sigmoids to infer twist and magnetic-energy content (Titov & Démoulin 1999). Using a time-slice method, the twist can be indirectly inferred from the observed unwinding motions of erupting jets and filaments, which reflect helicity release (Yan et al. 2014; Liu et al. 2009). In this work, we aim to provide a method for the estimation of the twist that is easily applicable in a space-weather framework. We first inspected how the variability of the twist influences the accuracy of the modelling results, and then we focused on deriving the range of magnetic twist for multiple CME events, most of which are associated with a flare eruption.

This paper is structured as follows. Section 2 describes the findings that motivated this study. Section 3 details the data used for the study and the description of the methodology. It is followed by the Section 4, in which we present an analysis of the MFR dataset. Statistical results are shown in Section 5. We summarise and discuss our work in Section 6. Appendices A and B provide the table of the studied events and the guidelines on how to use the developed tool for the twist estimation together with the required source code.

2. Case study: Impact of the twist parameter on the accuracy of the CME modelling

In this section, we discuss the influence of the twist input parameter on the accuracy of modelling with FRi3D. We aim to understand and quantify the impact of the twist in a case study of a CME on November 28, 2023.

A flux rope is generally described as an idealised configuration of a magnetic field with a local cylindrical geometry. A strong magnetic field on the MFR axis decreases radially towards the edges, and the twist increases with the radial distance (Russell 1999). However, recent studies show a correspondence of in situ measurements of field-line lengths with a MFR that has constant twist (Hu et al. 2015). According to this result, a constant twist for the construction of the 3D configuration of the magnetic field is implemented in the FRi3D model, where the twist is defined as the unitless number of turns in the magnetic field from one foot point of the flux rope to the other (see e.g. (Maharana et al. 2022)). Nevertheless, the estimation of the twist parameter for flux-rope CME models remains a challenge.

In the study of the CME on November 28, 2023, we used a range of twist values from 0.5 to 2.5, with increments of 0.1. All other CME input parameters were kept unchanged. The CME was first detected by the Large Angle and Spectrometric Coronagraph (LASCO, Brueckner et al. 1995) C2 instrument on board the Solar and Heliospheric Observatory satellite (SOHO, Domingo et al. 1995) at 20:24 UT. CME and CME-driven shock signatures observed among in situ data (retrieved from OMNI database[1]) were detected around 23:20 UT on November 30. The arrival of a shock was followed by a smooth rotation of the magnetic field consistent with a magnetic-cloud structure.

The results of modelling with FRi3D are shown in Fig. 1; they are colour-coded for different twist values. The plasma and magnetic-field in situ observations at 1 au are presented with a dotted black line. The results show that an increase in the twist leads to systematically faster CME propagation and, therefore, an earlier arrival time. Simultaneously with the increase of the CME speed, the solar-wind density decreases. The total magnetic field shows a complex time profile, which is somewhat different for different twist values. The twist increase initially induces an increase of the peak amplitude of the total magnetic fields. At a value of about $\tau = 1.0$, the peak amplitude starts to slowly decrease. The components of the magnetic field have very different time profiles, with By being the most complex one. The change in the twist results in a systematic change of the Bx component and a very complex behaviour of the other two magnetic-field components. Such results highlight the sensitivity of the CME magnetic structure to the twist parameter within the FRi3D model.

The parametric case study of the twist shows a difference of more than 20 hours for the arrival time, and a variation of up to 30% in the total magnetic-field strength. Such a large spread of values will induce substantial inaccuracy when modelling CMEs for the purpose of space-weather forecasting. These findings underline the importance of constraining the twist parameter for CME modelling within the space weather framework to (1) better reproduce the magnetic-field strength and preserve the structural fidelity of the modelled magnetic cloud; and (2) assert its influence on the arrival time of the ICME. Both aspects are vital

[1] https://cdaweb.gsfc.nasa.gov

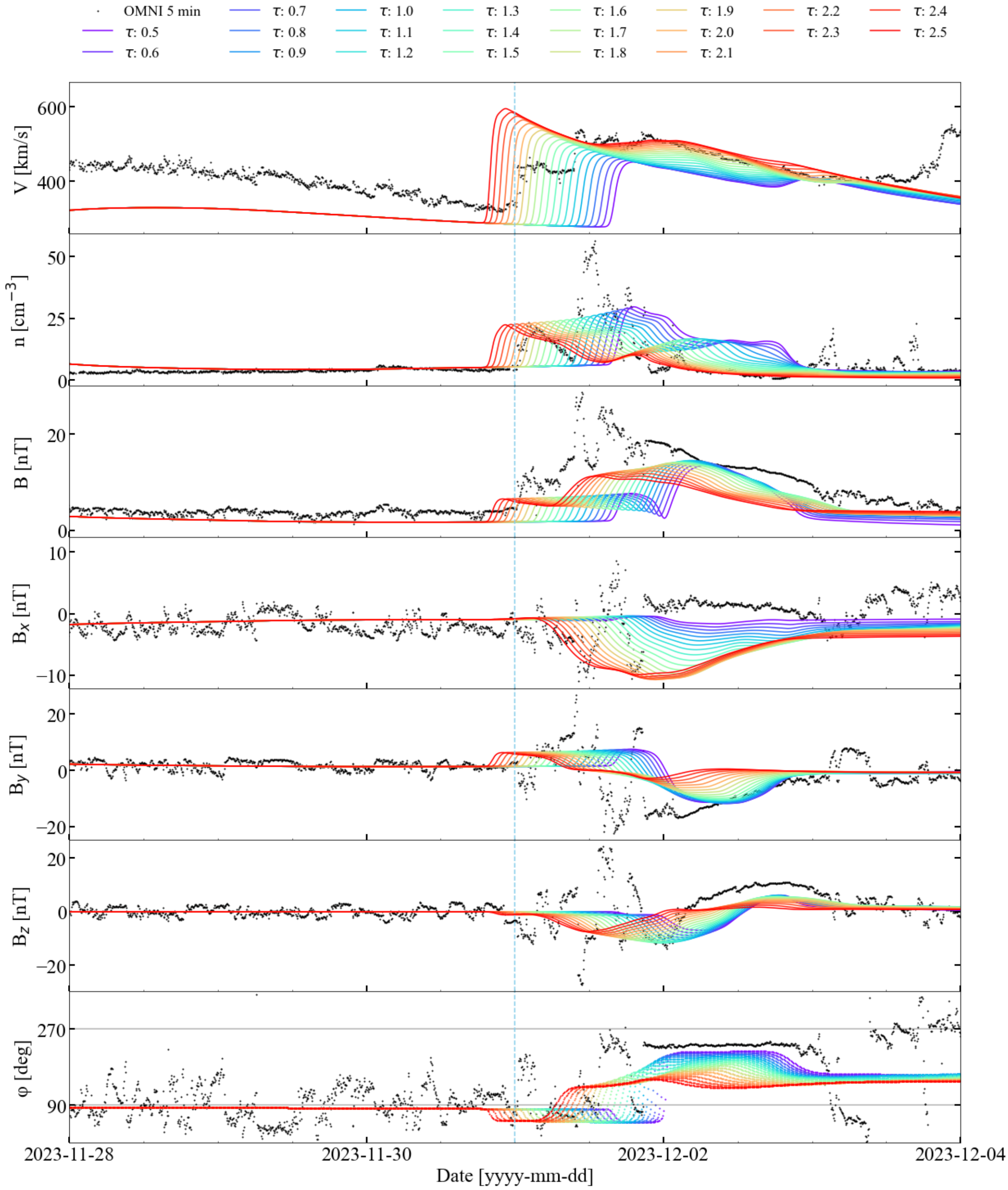

Fig. 1: Time series of plasma and magnetic-field properties at Earth are shown by a dotted black line with a five-minute cadence. The shock arrival and the CME end are marked with vertical dotted light blue lines, while the magnetic-cloud start is indicated by a vertical dotted grey line. The in situ observations are compared with the modelling results. The results of the CME modelled with FRi3D with different values of the twist parameter, τ, are presented in the colour-coded time series. Solar wind parameters from top to bottom: speed (V); density (n); total magnetic field (B); B_x, B_y, and B_z components in GSE coordinates; and the angle φ formed by the solar wind and the Sun–Earth line on the ecliptic plane.

in the forecasting of the geomagnetic impact of the CME and CME-driven shock. As CME input parameters to the model are derived from observations and/or empirical results, we aim to provide a method to estimate the twist parameter from solar observations routinely employed in space-weather forecasting.

3. Data and methodology

3.1. Observations

For the estimation of the twist we primarily used extreme ultraviolet (EUV) images from the Atmospheric Imaging Assembly (AIA, Lemen et al. 2012) on board the Solar Dynamics Ob-

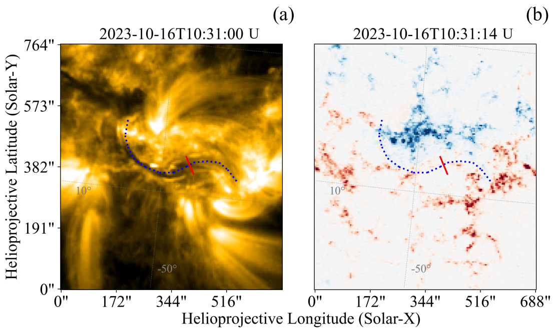

Fig. 2: Measurement of axial length (blue line) and the width (red line) of the flux tube from a selected EUV image/magnetogram pair. (a) EUV image form SolO/EUI in 174 Å. (b) SDO/HMI magnetogram.

servatory (SDO, Pesnell et al. 2012) at 171 Å. The SDO observations were combined with the Extreme Ultraviolet Imager (EUVI, Wuelser et al. 2004) from the twin Solar TErrestrial RElations Observatory (STEREO, Kaiser et al. 2008) spacecraft at 171 Å, or when not available at 195 Å. We also used the novel Extreme Ultraviolet Imager (EUI, Rochus et al. 2020) on board Solar Orbiter (SolO, Müller, D. et al. 2020); observations were taken at at 174 Å. The selected wavelengths are suitable for observations of the coronal loops and filaments associated with a MFR. Such an approach allowed us to consistently compare results obtained by different instruments observing from different viewing points. We also employed magnetograms from the SDO HMI (Helioseismic Magnetic Imager; Scherrer et al. 2012). The synoptic GONG (see e.g. Hill 2018) magnetogram maps were used as input for the modelling with EUHFORIA.

To calculate the speed and 3D geometry of the associated CME, we used the white-light images of the C2 and C3 instruments from the LASCO coronagraph, on board the SOHO mission. These observations were complemented with the white-light images of COR2 (SECCHI-Coronagraph Imager 2, Vourlidas et al. 2004) taken on board STEREO. To analyse the flare activity associated with the MFRs and CMEs we used data from the SXI (solar X-ray imager) taken on board the GOES (Geostationary Operational Environmental Satellite, Bornmann et al. 1996).

3.2. Estimation of the twist parameter

Changes in the twist parameter influence the CME modelling results, affecting the prediction of ICME arrival at Earth and magnetic-field strength, as presented in Section 2. Thus, the accurate estimation of the twist parameter is essential for reliable CME forecasting. In this section we present a geometry-based method to estimate the twist parameter from a selected EUV image.

The proposed methodology is based on the findings reported in Guo et al. (2021). The authors modelled the 3D MFR of five solar filaments using the regularised Biot–Savart law (RBSL) method (Titov et al. 2018). They obtained a quantitative relationship between the unsigned average twist of an MFR and its geometrical aspect ratio, L/a (L is the axial length and a is the minor radius of the flux rope). The empirical finding was tested using the Titov–Démoulin-modified (TDm) model (Titov et al. 2014) in conjunction with the RBSL method. They derived the linear relation expressed by Eq. 1:

$$\tau = 0.26(L/a) - 0.15. \quad (1)$$

We adapted Eq. 1 to estimate the L/a ratio from the EUV image. We employed EUV images because they provide information about low coronal structures and can be used in real time to measure the 2D geometrical properties of the MFR. It needs to be emphasised that the procedure we used to obtain the L/a ratio is different from that of Guo et al. (2021).

The JHelioviewer visualisation tool (Müller et al. 2017) was employed for the event analysis. JHelioviewer allows us to monitor solar activity and select data in close to real time, which is suitable for space-weather forecasting. First we inspected magnetic-field and EUV observations at different wavelengths (304, 211, 193, 174, 94 Å in both plain and running difference images) in order to understand the evolution of the studied event. Data were inspected from two different viewing points whenever possible (in 93% of cases out of 43 events). As for the estimation of the MFR characteristics, different coronal structures are important. We inspected the evolution of dimmings, flare ribbons, and filament eruptions associated with the event (see e.g. James et al. 2017). Only after understanding (as well as possible, depending on the complexity of the event) the full picture of the event were the characteristics of the MFR estimated as visible in Fig. 2.

The time frame that better displays the MFR in EUV observation was selected. It was observed in the multi-wavelength data that MFRs can experience significant changes before culminating in an eruption (see e.g. Duan et al. 2021). Therefore, we selected a time frame close to and prior to the eruption, before major changes in the structure are observed. Together with the EUV image, we also inspected the closest available magnetogram in time in order to better understand the position of the polarity inversion line (PIL) in the active region and the position of the MFR footpoints. Following the procedure we drew the line in the 2D space marking the axial length and width of the MFR on the EUV image. Fig. 2 illustrates this procedure and shows observations of an eruption on October 16, 2023. We noted that the CME source region was located approximately 7° west of the Sun–SolO line. The left panel shows the EUV time frame from SolO/EUI data. The longitudinal distance of SolO was 55.8° east of Earth. The SDO/HMI magnetogram, used to aid in the identification of the location of the footpoints, is shown in the right panel of Fig 2. The axial length is defined by a series of straight segments, denoted by the dotted blue lines, connecting from one footpoint of the MFR to the other. The MFR width is marked by a single straight redline. The measurements were taken using an interactive tool developed specifically to estimate MFR twist (see Appendix B) and available in Zenodo.

We compared the results of four events analysed in Guo et al. (2021) with our results. We only used four out of five events described in that paper since one filament was a confined event, and our study focuses on MFRs associated with CME eruptions. Table 1 presents the aspect ratios derived by both procedures. In the 3D study, the authors considered two values for the minor radius a; hence, we have two columns for comparison. The initial 2D estimates of the ratio using Eq. 1 resulted in higher values than expected. By taking a as half of the measured width we obtained ratios approximately double those resulting from the 3D reconstructions (2D and 3D columns, respectively). This difference, i.e. the underestimation of a, highlights the limitations arising from the 2D approach in which we considered the projected appearance of the associated filament observed in EUV images.

Table 1: Resulting ratios calculated for four events with 3D reconstruction (second and third columns), with the 2D estimation (fourth column) and the modified 2D estimation (fifth column).

	L/a			
Event	**3D**		**2D**	**2D corrected**
2010/08/07	10.6	9.4	20.6	10.3
2011/07/09	19.3	17.2	35.0	17.5
2012/05/05	8.6	8.9	17.9	8.9
2012/05/10	17.3	14.7	31.5	15.7

We therefore modified the method by taking the full width of the MFR as the value for a, rather than the minor radius. We name the obtained values as the 2D-corrected L/a ratio (right column, Table 1). The revised ratios exhibit better agreement with the results from the 3D approach. Although filaments are a good proxy to understand the structure and location of MFRs, they do not necessarily fully represent their often complex topology, which induces some uncertainties regardless of the twist estimation method.

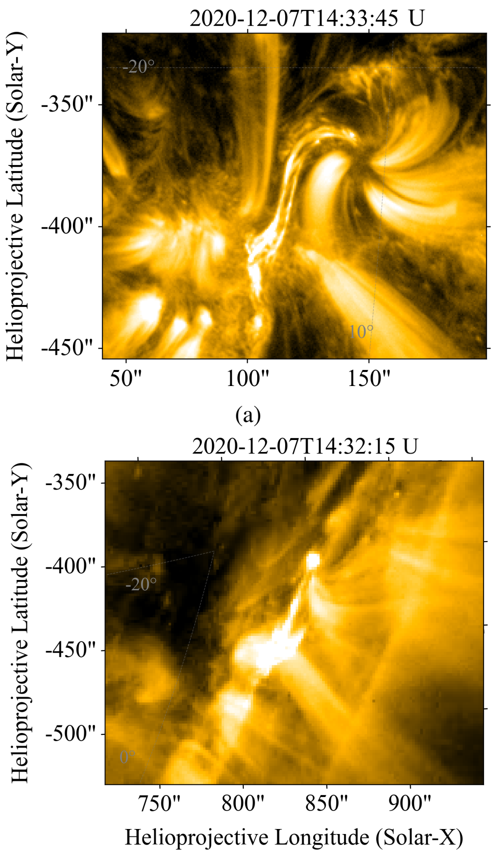

Fig. 3: Observation of a MFR by two different spacecraft. For the SDO/AIA instrument (a), the MFR is observed between 100" and 150" relative to the spacecraft; while for the STEREO-A/EUVI instrument (b) it is between 800" and 850" relative to the spacecraft. The 2D geometry changes depending on the field of view.

Depending on the viewing angle, the apparent geometry of the structure can differ significantly. Fig. 3 shows a MFR in EUV observations at 171 Å from two different viewing points. The considered images were taken before the eruption on December 7, 2020. The top panel shows the viewpoint from SDO/AIA between 100" and 150" in helioprojective longitude, while the bottom panel shows the viewpoint from STEREO-A/EUVI between 800" and 850" in helioprojective longitude. When observing the filament structure from close to the central meridian an S-shaped form is often found (e.g. top panel of Fig 3). On the other hand, for structures seen from close to the limb the s shape is not distinguishable, and a more line-like form of the filament is observed (bottom panel of Fig 3). It is therefore essential to assess the impact of the projection effects on the estimation of the twist; this is presented in detail in Section 5.

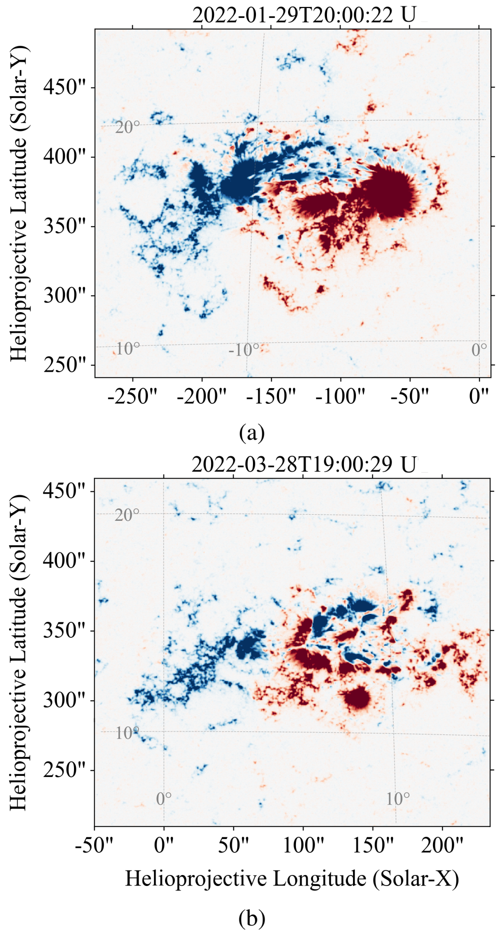

Fig. 4: HMI magnetogram of NOAA AR 12936 (a) and of NOAA AR 12975 (b). AR 12936 presents a clear distinction between the polarity regions, while AR 12975 shows a more complex magnetic configuration.

Magnetogram observations are valuable as complementary data, in particular when the source region exhibits high magnetic complexity. The clarity with which positive and negative polarity areas are defined directly affects the accurate identification of the MFR footpoints and, consequently, the determination of its axial length. In such a case of mixed polarities and unclear footpoints ambiguity and error in estimating L can occur. On the other hand, a well-defined PIL, which often lies below the axis of the MFR (Marubashi et al. 2015), provides a valuable morphological reference to locate the flux-rope channel. Accurate identification of the PIL is of particular importance when the structure in EUV is not clearly defined. In Fig. 4 the SDO/HMI magnetograms of two fully developed ARs are compared. In the region shown in the top panel, there is a clear distinction between positive and negative polarity, and therefore the MFR footpoints and the PIL are easily defined. In contrast, the region shown in the bottom panel exhibits a more complex configuration, with positive and negative areas mixing. Thus, it is more difficult to locate the position of the footpoints, which increases the uncertainty in the estimation of the twist.

4. Event descriptions and measured quantities

In this section we present the measurements and observations used for the statistical study. In order to ease the reading and its flow, we show the table with information about the studied events in Appendix A.

We used the proposed method to estimate the twist for 43 MFRs. The measurements were performed using the structure observed in the single selected EUV image per event. It is known that different wavelengths reveal different characteristics of solar magnetic structures. Therefore, it is inherently difficult to map the entire solar magnetic structure regardless of the wavelength used. Having all this in mind, we selected wavelengths which provide good mapping of the coronal structures and allow the comparison of observations from different spacecraft. For this study, we used SDO/AIA 171 Å, STEREO-A/EUVI 171 Å and 195 Å, and SOLO/EUI 174 Å. Each event is associated with a CME eruption and, in most cases, with solar flare.

We differentiated between events with a clear PIL and those with a complex PIL (marked in column 1, Table A.1 with an asterisk). The complexity of the PIL is directly associated with the magnetic-field complexity of the part of the active region/s that sourced the eruption. Accurate PIL identification remains critical during CME 3D reconstruction for the estimation of the speed and orientation of the CME. The orientation and morphology of the CME are directly related to the initial direction and tilt of the eruption, which rely on the PIL. In cases where the PIL is diffuse or irregular, uncertainty increases in defining the propagation direction of the CME.

We estimated the CME speed V_{CME} (column 10, Table A.1) by performing a 3D reconstruction using a white-light fitting tool that incorporates the geometry of the FRi3D model. The FRi3D CME model has more free parameters and a more deformable geometry, which allowed us to incorporate any major alterations a CME can undergo and therefore represent more realistic CMEs.

All the CME reconstructions were performed using the coronagraph images from SOHO/LASCO/C2 and SOHO/LASCO/C3 combined with the STEREO-A/COR-2 images. We used five pairs of images, trying to focus on the later phase of the CME propagation in the coronagraph field of view. This approach was adopted in order to obtain the CME speed as accurately as possible at distances close to the insertion domain in EUHFORIA, i.e. 0.1 au, and to avoid the distances closer to the Sun at which the CME could still significantly change its speed (Valentino & Magdalenic 2024). Similarly to the GCS (Graduated Cylindrical Shell; Thernisien 2011) model, this tool uses coronagraph observations of CMEs to map their 3D morphology, position, and speed. The FRi3D CME reconstruction provides the mapping of the CME morphology and the flux-rope characteristics, which are not available with the GCS and are needed for the CME modelling with FRi3D. In order to calculate the CME speed, two or, ideally, more coronagraph images are necessary.

Figure 5 shows two examples of the 3D-CME reconstruction for one snapshot. The first example (Fig 5a) corresponds to event E9. The CME is visible as a halo in SOHO/LASCO images and as a partial halo in STEREO-A/COR-2 images. This CME had a geomagnetic impact at Earth with the Kp-index (Kp), which defines the level of the impact equal to six. The event E9 is a clear example of the deformation of a CME due to expansion and interaction with the ambient coronal structures. The FRi3D deformation parameters (marked by light blue arrows) allow for a more precise reconstruction of this distorted CME geometry. The widening of the CME legs and a consequent squashing of the CME leading edge is visible in subsequent coronal images while fitting the MFR with the FRi3D tool. The flattening parameter allowed us to model these CME dynamics better than GCS. A clear decrease in the thickness of the leading edge, which can be characterised by the pancaking parameter, is also observed. A more detailed description of the deformation parameters can be found in Maharana et al. (2022). The second example shown in Fig 5b corresponds to event E37. The CME eruption was associated with the X1.84 flare, a solar energetic particle (SEP) event, and a strong geomagnetic perturbation characterised by a Kp = 8+. The CME is visible as a halo in both SOHO and STEREO-A, which makes a 3D reconstruction more difficult. For this event it was possible to identify the main magnetic structure of the CME, i.e. the CME core, the cavity, and the leading edge (marked by green arrows in Fig 5b). This allowed us to understand that the bright structures, visible close to the CME legs in both coronagraph images, are not part of the CME itself but the nearby coronal structure of streamer.

We noted that for MFR event E39, although a patchy and faint flow-like structure is visible in running-difference coronagraph images, we were not able to not estimate the velocity of the CME. The EUV wave associated with the GOES C7.1 flare and MFR propagated northward from the source region, indicating that the faint signatures visible in the coronagraph images are possibly CME signatures.

The majority of studied MFR events were observed by two or more spacecraft simultaneously. Observations from the point of view (POV) of Earth were ensured for all cases. Out of 43 MFR events, 23 were observed by SDO, STEREO, and SolO missions; 17 were observed by SDO and STEREO; and three were only observed by SDO. Such a composition of our dataset is important because multiple viewpoint observations are essential for assessing the projection effect in twist estimation. For each event and POV, we performed five measurements and obtained the average value of the twist, τ, and its standard deviation (column 5, Table A.1). The location of the structure on the solar disc was defined by its absolute longitude relative to the observing spacecraft (column 6, Table A.1). The average measured length and width of the MFR, from the different POVs, were also estimated and are listed in columns 8 and 9 of Table A.1, respectively.

The multi-viewpoint observations provided information concerning the MFR at different longitudes. That gave us the possibility to focus on the influence of the projection effect on the estimate of the twist. For each event, we de-projected τ to the central meridian as seen from each individual spacecraft and obtained the de-projected value τ_d. The de-projection was calculated by applying Eq. 3, which relates τ to the position in longitude of the source region relative to the spacecraft. We considered longitude = 0° as the central meridian. The derivation of Eq. 3 is detailed in Section 5. The de-projection of the twist value characterising each event is important for a further consistent study of the relationship of τ with other properties associated with the MFR. Both projected and de-projected values, i.e. measured and

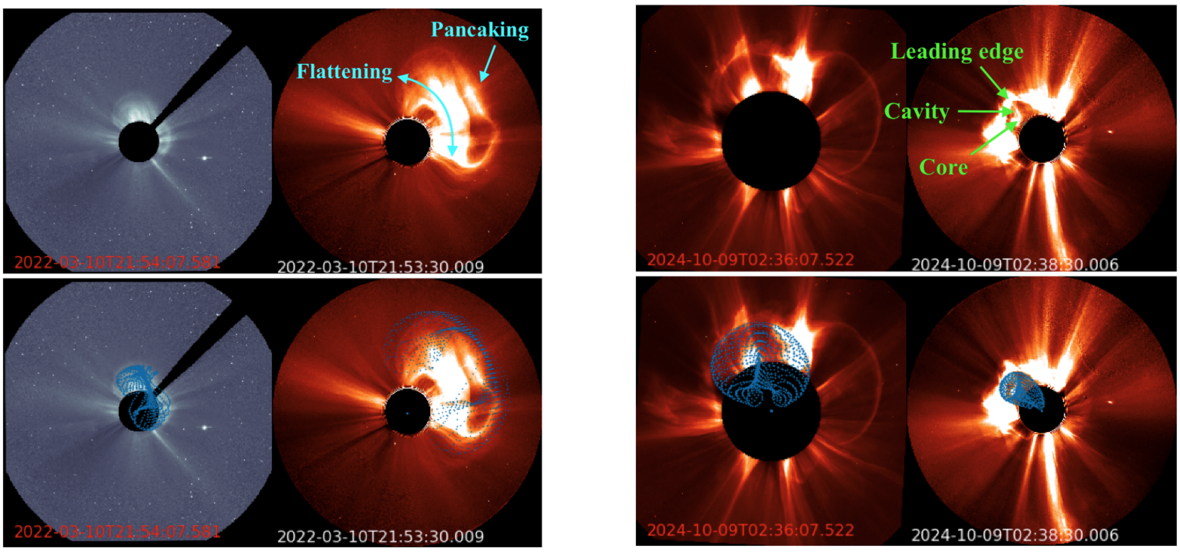

(a) (b)

Fig. 5: Example of 3D CME reconstruction for two CME events. The reconstructions were done using multi-viewing coronagraph white-light images. One snapshot of the 3D CME reconstruction is shown for each event. (a) CME associated with the MFR event E9. The SOHO/C3 coronagraph image is shown on the left and the STEREO-A/COR-2 one on the right. The blue arrows indicate the main CME deformations that can be shaped with the pancaking and flattening FRi3D parameters. (b) CME associated with MFR event E37 is shown in SOHO/C2 coronagraph image on the left and STEREO-A/COR-2 on the right. The green arrow in the top panel describes the main features of the CME observed in white light: the core, the cavity, and the leading edge; these are key for an accurate orientation of the structure and 3D reconstruction.

calculated values of the twist, are listed in Table A.1, columns 5 and 7, respectively.

Columns 11, 12, and 13 in Table A.1 list the flare magnitude, the NOAA AR number, and its Hale magnetic classification, respectively. For MFR event E31 the source region is located at the east limb, as seen from all three spacecraft, and at the time of the MFR eruption it was not yet numbered. Moreover, no flaring activity from this region was registered. The second event that had no associated flare and also no numbered AR was a quiescent eruption, the MFR event E32. Two more particular MFR events with unclear source regions were E38 and E40, which were associated with a flare occurring between two ARs. E38 occurred between NOAA AR 13852 and NOAA AR 13854, and the GOES M2.14 flare was attributed to AR 13854. E40 occurred between NOAA AR 13961 and NOAA AR 13962, and the GOES M1.35 flare source region was attributed to AR 13961.

5. Statistical results

In this section we first discuss the measurement of the MFR twist, τ, obtained from different viewing points and the derived de-projected MFR twist, τ_d. The variability of the τ_d is then addressed in the context of the associated CME and flare events and their characteristics.

5.1. Influence of projection effect on the twist

In order to study the MFR twist, τ, when using data from different viewing points, we selected a subset of 23 out of the 43 events by retaining those observed by three spacecraft (SDO, STEREO-A, and SolO). The measured twist for 23 selected events, viewed from different spacecraft (column 6 versus column 5 of Table A.1), is shown in Fig. 6 as a function of the relative absolute longitude. The events are colour-coded and the measurements from different POVs, for individual events, are connected by lines. This presentation combines the relative position of the flux rope with respect to the observer and the twist value, which is also a crucial factor in interpreting the morphological features of the flux rope observed in the EUV images.

We found a clear and consistent dependence of the estimated magnetic twist on the vantage point of the observer, indicating a strong influence of projection. In the majority of cases, the estimated twist is larger when the observer views the structure near the disc centre at a relative longitude of 0°. A systematic decrease is observed when the structure is viewed closer to the limb, at a relative longitude of ±90°. The grouping of the three points per event provides a qualitative indicator of this projection-induced variation. The slope of the connecting lines is predominantly negative, indicating the general trend of decreasing twist with increasing longitude. We further described the trend by a two-step linear regression. First, we performed individual fits to the twist–longitude relation for each event. Then, we averaged the individual fits to produce a single fit that represents the complete dataset. The fitting is presented as a dashed black line in Fig. 6 and described by Eq. 2:

$$\tau = -0.02Lon + 2.52. \tag{2}$$

The example of significantly changed magnetic structures in EUV observations, depending on the viewing angle, was presented in Fig. 3. When observed at the disc centre the MFR "true" axial length and the cross-section width can be measured,

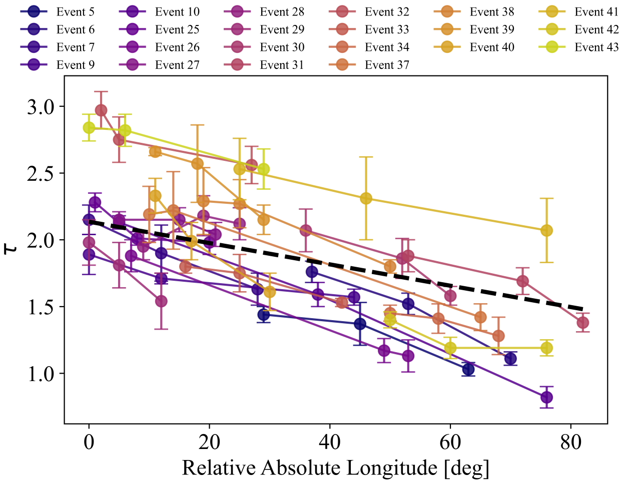

Fig. 6: Measured τ value as a function of relative absolute longitude for a subset of 23 out of 43 events. Each colour-coded event was observed from three different vantage points. The events are numbered according to Table A.1. The measurements from a different view point are connected by a straight line. Error bars represent the standard deviation of the measurement. The dashed black line shows the average linear regression fit across all events.

enabling the most reliable determination of the L/a ratio, and thus also the MFR twist. To account for projection effects across varying viewpoints, we de-projected all twist measurements to the central meridian ($Lon_f = 0°$) relative to the spacecraft. We used Eq. 3:

$$\tau_f = \tau_i - 0.15\left(\frac{Lon_f - Lon_i}{10°}\right), \quad (3)$$

which is the general form of Eq 2. The parameters τ_i and Lon_i represent the initially measured twist and relative longitude of the observer, respectively. To correct for dimensionality we divided ($Lon_f - Lon_i$) by 10°. The de-projected twist values from all available viewpoints for a given event were averaged to obtain a single representative twist per event, which we defined as τ_d (column 7 in Table A.1). This procedure ensures a consistent basis for comparing the twist values in subsequent analyses.

5.2. Twist association with CME speed and flare energy

The association between fast CMEs and low twist values was rarely discussed in the past (see e.g. Hu et al. 2015). Therefore, in this study we aim to provide a more comprehensive understanding of the relationship between the CME characteristics and the twist values. As the solar flares and CMEs are closely associated phenomena (e.g. Bein et al. 2012; Salas-Matamoros & Klein 2015, etc.), which are sometimes even considered to be two aspects of a complex energy and magnetic-field-release process, we decided to also include the flare characteristics in our study. We studied the variation of the de-projected twist value, τ_d, in relation with the CME speed and flare activity.

The left-hand column of Fig. 7 shows the dependence of τ_d on the variation of the CME speed for the full dataset (panel a) and two subsets (panels b and c). The information on the flare energy size is colour-coded according to a logarithmic scale. Additionally, to ease the understanding of the plots, we marked the GOES flare classification with different symbols: circles, triangles, and squares for C-, M-, and X-class flares, respectively. A second-order polynomial fit was performed without taking into account the different flare sizes. We calculated the correlation (C) and the 95% confidence interval (CI) of the polynomial fit using a t distribution. The CI is indicated by a grey shaded area. This type of distribution accounts for the increased uncertainty associated with small sample sizes and provides a more reliable estimation of the interval than assuming a normal distribution.

The right-hand column of Fig. 7 shows the assessment of the robustness of the correlation when applying bootstrap resampling (see e.g. Dissauer et al. 2018) to C value, for the same datasets as in the left-hand column. This non-parametric method is particularly well suited for small datasets, and it does not include assumptions about the underlying distribution of the data. By repeatedly resampling the original dataset and recalculating C, the bootstrap approach enables an empirical estimation of its uncertainty and provides a data-driven 95% CI, delivering a rather reliable evaluation of the correlation strength. All three distributions are made of the C values from 10.000 bootstrap samples, with the mean C and 95% bootstrap CI marked by vertical dashed red and green lines, respectively.

Table 2 summarises the results of the C value for the polynomial fits, the mean bootstrap C, and the 95% CI derived from the bootstrap distributions for the full dataset and all the discussed subsets. We first analysed the complete dataset (Fig. 7a), with the exception of the three cases without associated flares, which consisted of 40 events. The twist decreases with increasing CME speed up to about 900 km/s and then increases for the faster CMEs. The 95% CI around the fit, marked with grey shaded area, indicates notable uncertainty. The C value of the polynomial fit is 0.65 and the bootstrap distribution of the C value has a comparable mean correlation of 0.66 (marked with a vertical dashed red line) and a 95% CI of 0.376–0.846 (marked with vertical dashed green lines). The bootstrap distribution shows correlation with moderate but coherent spread, which indicates association between the CME speed and the MFR twist, with observable but not very large uncertainty.

The events associated with more energetic flares, i.e. X-class flares, seem to be scattered from the fit (blue shaded square symbols in Fig. 7a). Therefore, we excluded the events associated with X-class flares and repeated the analysis on the rest of the dataset (Fig. 7b). This reduced the dataset to 33 events associated with C- and M-class flares. Such an approach provides better correlation between studied variables and a more accurate quadratic trend. The obtained fit maintains the same U shape with the lowest twist values, i.e. the saddle point, around the CME speed of 900 km/s. The C value of the polynomial fit is improved to 0.83, as well as the bootstrap mean C value. The bootstrap 95% CI also improves, and it is in the range of 0.674–0.927. These improvements in both the C and the confidence interval show that the relationship between τ_d and V_{CME} is significantly better pronounced for events associated with the low-energy flares.

We further studied the events associated with X-class flares separately in order to better comprehend their impact within the full dataset (Fig. 7c). This sample is rather small, with only seven events, which possibly reflects in the polynomial fit value of C being only 0.49. The 95% CI is broader than for the subset of the C- and M-class-flare-associated events in the CME speed range, which is only a fraction of the full speed range presented in panels a) and b) of Fig. 7 (marked with the blue line). The bootstrap results show a correlation of a similar value to the full dataset (panel a) and a higher correlation than the associated polyno-

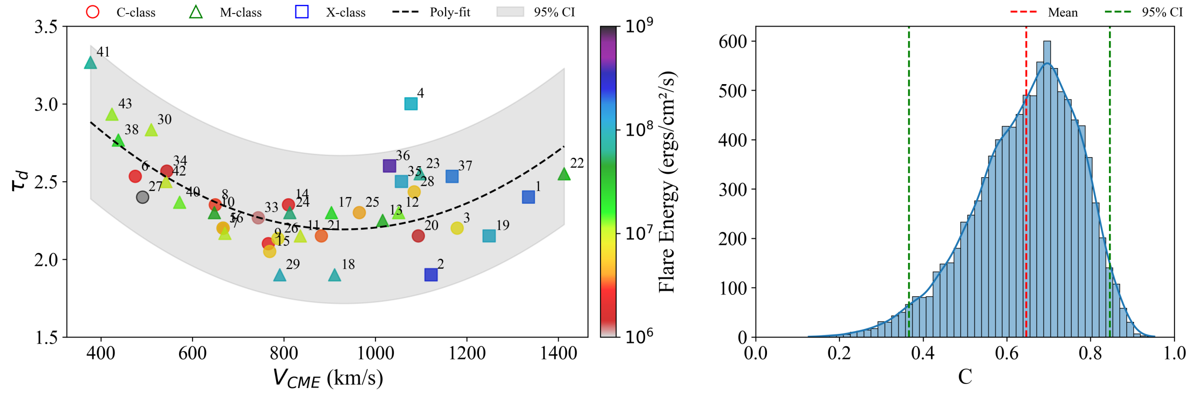

(a)

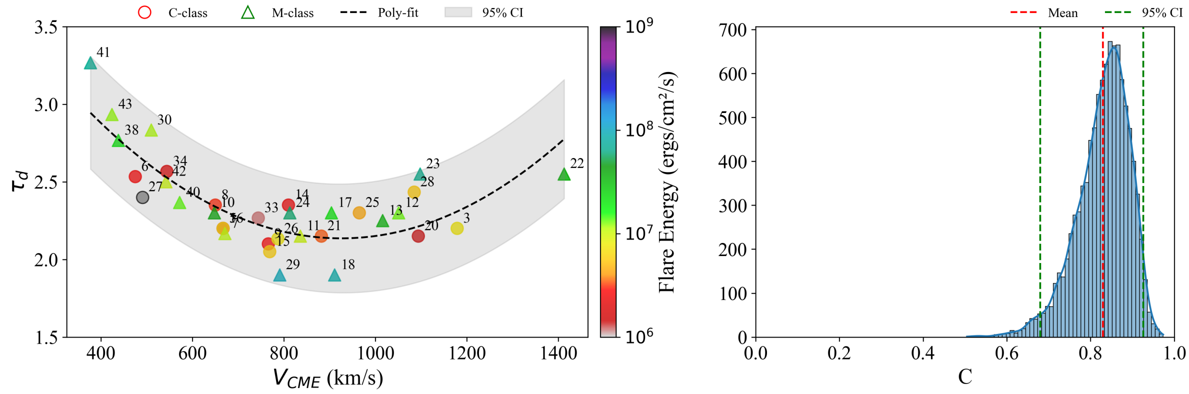

(b)

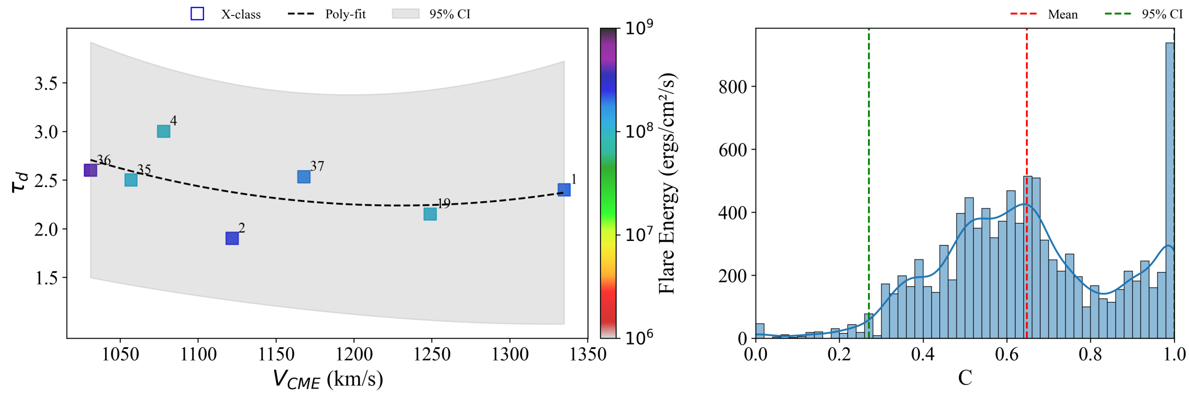

(c)

Fig. 7: *Left panels*: Dependence of τ_d on the variation of V_{CME}. The flare energy size is colour-coded according to a logarithmic scale. The flare GOES classification is marked with symbols: circles, triangles, and squares for C-, M-, and X classes, respectively. The dashed black line defines the polynomial fit and the grey area the 95% confidence interval, *CI*. The event number is labelled. *Right panels*: Bootstrap distribution of correlation (C) value for 10.000 empirically based samples; the mean C value and the 95% *CI* of the distribution are defined by vertical dashed red and green lines, respectively. *From top to bottom*: (a) Full dataset of events with an associated flare eruption (40 cases); (b) subset of events with associated C- and M-class flares (33 cases); (c) subset of X-class-flare-associated events (7 cases). The blue horizontal line in the left panels (a) and (b) indicate the CME speed range for the subset in panel (c).

mial fit value C. The bootstrap mean C rises to 0.68 but presents an extremely wide 95% *CI* of 0.27–1.0. This emphasises that the correlation for X-class events remains not well defined, possibly as a result of the small sample size. Even though the bootstrap mean C value is comparable to that of the full dataset, the functional relationship between CME speed and MFR twist in the events associated with the X-class flares is different from that of the full dataset and the subset of events associated with C- and M-class flares.

In Fig. 8a we superpose the polynomial fits that shape the three subsets of events presented in Fig. 7 in order to more transparently compare the fits and their *CIs* (see also Table 2). The magenta curve corresponds to the full dataset, the orange curve to the events associated with C- and M-class flares, and the blue curve to the events associated with X-class flares. The shaded areas correspond to the 95% *CI* associated with the polynomial fit, while the *C* values shown on top are the mean values obtained from the bootstrap analysis. Although the subset of X-class-associated events exhibits a noticeably different behaviour, the fit of the subset of C- and M-class associated events remains closely aligned with that of the full dataset. We note that the *CI* for the subset of the X-class-associated events is at least three times larger than in the case of the other two subsets. This shows that the overall relationship between τ_d and V_{CME} is predominantly shaped by the C- and M-class-associated events, and is only weakly influenced by the inclusion of the X-class-associated data.

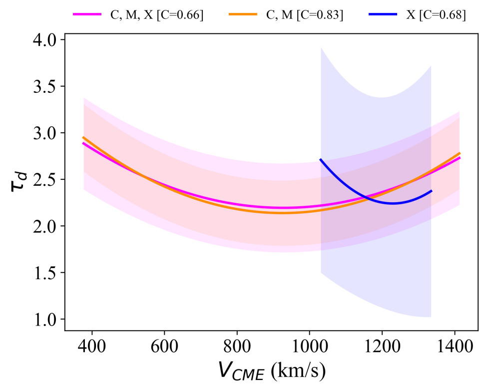

(a)

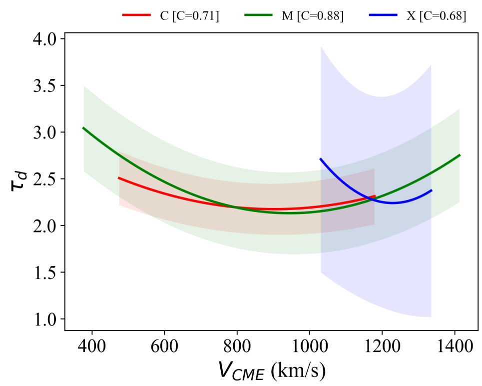

(b)

Fig. 8: Overlapped second-degree polynomial fit of (a) the full dataset (magenta), C- and M-class-flare-associated events (orange), and X-class-associated events (blue); (b) C-class-flare (red), M-class-flare (green), and X-class-flare (blue) associated events. Shaded regions indicate the 95% *CI* of each fit as derived from the *t* distribution. The *C* values correspond to the mean *C* bootstrap result for the subsets.

By studying subsets of events according to their association with the different flare classes, we can better understand how individual flare-associated groups contribute to the overall trend in the relationship between τ_d and V_{CME}. Fig. 8b shows the second-degree polynomial fit and the 95% *CI* for the C-class (red), M-class (green), and X-class (blue) flare-associated events (see also Table 2). The subset of events associated with C-class flares encompasses a rather small range of the MFR τ_d values for the full range of the CME speeds, which is also reflected in the broad range of the 95% bootstrap *CI* of 0.342–0.903. Figure 8b shows that the range of the MFR τ_d values for the M-class-associated events extends to lower and higher values in comparison with C-class fares. Accordingly, the fit of M-class-flare-associated events fully covers the range of the C-class flares. Since the dynamical range of the M-class events is larger, this reflects in the significantly narrower range of the 95% bootstrap *CI* (0.699–0.971) and, in general, the better correlation (mean bootstrap *C* value of 0.88) between the MFR τ_d values and V_{CME} (see also Table 2). Fig. 7b shows that the saddle part of the fit (range of the CME speeds 600–1100 km/s) is mostly populated with events covering the narrow range of MFR τ values, the majority of which are associated with the C-class events. However, the bootstrap method shows that the events outside of this range, with MFR τ values below 2 and above 2.5 are statistically significant, which is visible in the large $C = 0.88$ value for the M-class events. The rather close agreement between the correlation for the τ and V_{CME} in the case of the two subsets associated with the C-class and M-class events justifies grouping these two subsets into one. In contrast, the X-class subset exhibits a strongly different curvature with broader uncertainty, consistent with the more scattered behaviour discussed previously. Overall, this breakdown of the τ and V_{CME} relationship underscores that lower energy flares not only contribute meaningfully to the global correlation, but may also offer a more stable observational foundation for trend identification.

Table 2: Resulting correlation, *C*, derived from the polynomial relations (Poly-fit column) for the different considered subsets. Mean *C* value and 95% *CI* obtained from bootstrap analysis (Bootstrap columns).

Sample Group	**Poly-fit** *C*	**Bootstrap** *C* (Mean)	**Bootstrap** 95% *CI*	**Count**
C-M-X	0.65	0.66	0.365 - 0.845	40
C-M	0.82	0.83	0.677 - 0.928	33
X	0.49	0.68	0.271 - 1.000	7
M	0.86	0.88	0.699 - 0.971	17
C	0.68	0.71	0.308 - 0.907	16

Table 3: Values of the polynomial coefficients *a*, *b*, and *c* for all considered subsets.

Sample Group	***a***	***b***	***c***
C-M-X	0.16	-0.11	2.21
C-M	0.16	-0.20	2.20
X	0.12	-0.20	2.32
M	0.21	-0.28	2.22
C	0.08	-0.09	2.20

After establishing that the dependence of τ_d on the variation of V_{CME} is rather well defined by a second-degree polynomial fit, we derived the fit using a normalised value of the CME speed in order to correct dimensionality. The general form of the relationship for the three subsets is shown by Eq. 4:

$$p(x_{norm}) = ax_{norm}^2 + bx_{norm} + c$$
$$x_{norm} = \frac{x - \overline{x}}{\sigma}, \quad (4)$$

where x_{norm} is the normalised CME speed, x the measured V_{CME} value for a CME event, and $\overline{x}$ and σ the respective mean V_{CME} value and standard deviation of the dataset presented in this paper. The values of the coefficients *a*, *b*, and *c* for the full dataset and the considered subsets are presented in Table 3.

We conclude that the relationship obtained for the C- and M-class-associated events is characterised as follows:

$$\tau_d(V_{norm}) = 0.16\ V_{norm}^2 - 0.2\ V_{norm} + 2.2$$
$$V_{norm} = \left(\frac{V_{CME} - 776\ km\ s^{-1}}{243\ km\ s^{-1}}\right), \quad (5)$$

which can be employed as the observational based proxy for the estimation of the τ_d needed in the modelling of the CMEs. We note that, contrary to the τ_d, the CME speed is a parameter that can be easily estimated using the white-light observations.

6. Summary and discussions

Understanding the twist of MFRs is essential for characterising the evolution and geo-effectiveness of CMEs and their accurate modelling for scientific purposes and operational space weather. In this paper we present a comprehensive study of the estimation of the magnetic twist of solar eruptive structures, all the way from tool development to observational application and statistical analysis.

The case study of a CME on November 28, 2023, which showed the importance of the twist variability in accurate modelling with FRi3D, was the driver for the statistical study of the MFR twist and the development of the method for twist estimation. The results of this parametric study using τ values from 0.5 to 2.5 show a difference of more than 20 hours in the arrival time and variations of up to 30% in the magnetic-field strength at 1 au. This inaccuracy in modelling CMEs stresses the need for a systematic study of MFR twist.

The majority of the presently available methods for twist estimation are not easily integrated into time-sensitive space-weather-forecasting workflows. They often involve time-consuming analysis and high-quality vector magnetic data (see e.g. Wiegelmann 2004; Murray, M. J. & Hood, A. W. 2008; Titov & Démoulin 1999). In a real-time space-weather-forecasting context, decisions are time sensitive, and straightforward methods to estimate the key CME parameters are necessary. To address this need, we propose a method that is easily integrable into a space-weather operational workflow for the estimation of the MFR τ parameter. Our method is based on the work of Guo et al. (2021), in which the estimation of τ was derived from the ratio L/a, with L being the axial length and a the minor radius of the associated MFR in 3D. We employed EUV images from STEREO, SDO, and SolO to obtain the 2D geometrical properties of the MFR. As the minor radius of the MFR is rather difficult to measure, we obtained the MFR width and calculated a. We then tested the results of our 2D method on the events studied by Guo et al. (2021) in 3D. The comparison shows that twist values from our 2D study were about two times larger than those obtained by Guo et al. (2021). The largest influence on our estimate of the twist is probably due to uncertainties in the measurement of the MFR width, which results in the underestimation of the parameter a. In order to compensate for this effect, we multiplied the values of the minor radius, a, by two, which provided τ values similar to those of Guo et al. (2021).

We developed an interactive tool to estimate the twist of flux ropes by simultaneously combining EUV images with magnetogram data (see Appendix B). The method relies on measuring the geometrical properties of the MFR from which the twist is calculated using Eq. 1. The tool is designed to be user friendly and time-efficient. It is publicly available for the community in Zenodo.

We note that the 2D approach has two limitations that should be taken into account when performing the twist estimation: (a) the influence of the projection effects; and (b) the magnetic complexity of the source region, which can affect the accurate identification of the footpoints and the PIL.

In a statistical study of the MFR twist performed on the set of 43 MFR events, we tried to address these limitations. We used a subset of 23 events, which were observed simultaneously from three different vantage points in order to study the projection effect on τ estimation. We found a clear and consistent dependence of the estimated τ values on the viewing point. A systematic decrease of τ is observed when the flux-rope structure is seen closer to the solar limb.

This trend persisted for all spacecraft considered, which indicates that the projection bias arises from geometric distortion rather than instrumental limitations. The resulting composite fit across events exhibited a consistent negative slope, suggesting that the projection effect introduces a reproducible longitude-dependent bias and not randomly scattered values. To account for this, we empirically derived a linear regression model to adjust measured values obtained from the close-to-the limb regions, and we de-projected the twist, τ_d, to the reference value at the central meridian. This correction step is essential to ensure internal consistency across the event sample for further statistical study. The projection correction also supports the broader implementation of this method in operational contexts where single-viewpoint observations are normally available. We note that the spacecraft have different spatial resolutions, which do not influence our results. Namely, the size of the pixels in different spacecraft is at least one order of magnitude smaller than the average size of the a and L parameters.

After the de-projection, we inspected the dependence of τ_d on the variation of the 3D CME speed and the flare size. This association has rarely been discussed in the past, and our results provide the first comprehensive analysis of an extensive dataset. The initial analysis of the full dataset showed a correlation of τ_d with CME speed, with a moderate but coherent spread described by a quadratic function. The twist value decreases with increasing CME speed up to about 900 km/s. This behaviour changes in the case of fast CMEs for which the value of τ_d increases. The bootstrap distribution of the correlation C has a mean value of 0.66 and a 95% confidence interval CI of 0.376 - 0.846. The result suggests a clear association between the CME speed and the MFR twist with a rather low uncertainty.

Events associated with more energetic flares, i.e. X-class flares, seem to be rather widely spread around the fit. We therefore excluded those events and repeated the analysis on the rest of the dataset (total of 33 events). The subset of the C- and M-class-associated events shows better correlation between the studied variables and a more accurate quadratic trend. The obtained fit maintains the saddle point around the CME speed of 900 km/s. The bootstrap mean C value improved to 0.83; the 95% CI, which presents a visibly narrower range of 0.674–0.927 in comparison to the full data set, also improved. Such an improvement emphasises that the relationship between τ_d and V_{CME} is substantially better defined for events associated with the low-energy flares.

We studied the subset of events associated with the X-class flares separately. With a small sample of seven events, the polynomial fit shows a bootstrap mean C value of 0.68, but an extremely wide 95% CI of 0.270–1.000. This highlights that the relationship for X-class-associated events is not well defined, which is possibly a consequence of there being events. We note that the polynomial fit is different from that for the full dataset and for the subset of events associated with the C- and M-class flares.

The results from the subset of events associated with the C- and M-class flares suggests that within this energy range the twist of a MFR and the CME speed seem to be very closely associated. We conclude from such a promising result that the polynomial function obtained for this subset of events, given by Eq. 5, can be employed as an observation-based proxy for the estimation of τ_d from $V_{CME,}$ which is the CME parameter that can be easily estimated. This proxy is very valuable in a space-weather context, specifically because the direct measurement of the twist is often not possible. On the other hand, the near-real-time observations provide the possibility of a fast estimation of the CME speed.

We conclude that the statistical analysis revealed a strong correlation between MFR twist and CME speed, particularly in events associated with low to moderate flare energies. The empirical relation established here offers a practical diagnostic proxy for use in both post-event analyses and real-time forecasting environments. Our findings underscore the critical role of constraining the solar twist for CME modelling in scientific studies but also in the operational space-weather forecasting. We also derived a quantitative correction for projection effects in twist estimates based on EUV images, enabling more consistent cross-event comparisons. As outlined in Section 2 and at the beginning of this section, the driver for this work came from CME modelling performed with FRi3D in EUHFORIA, where the variation of the twist parameter significantly changed the arrival time and the magnetic-field strength predicted at Earth for E29. The measured average τ_d was 1.9 turns (see Table A.1), and the twist obtained from the proposed proxy was around 2.2 turns with a predicted range of 1.8–2.5 turns. The modelling results with FRi3D showed a similar arrival time to in situ observations for a twist in the range of 2.0–2.1. This consistency suggests that the observationally derived twist estimates can serve as reliable input for physics-based CME simulations. Future work will extend this approach to a broader set of events, aiming to systematically evaluate how the proposed method can be coupled with FRi3D and, more generally, to improve our physical understanding of CME dynamics and their space-weather impacts.

Data availability

The interactive tool used for the estimation of the magnetic flux-rope twist parameter, τ, is publicly available on Zenodo at `https://doi.org/10.5281/zenodo.15864359`.

Acknowledgements. B.D.D. gratefully thanks the Royal Observatory of Belgium (ROB) for the awarded Ph.D grant. The ROB team thanks the Belgian Federal Science Policy Office (BELSPO) for providing financial support within the framework of the PRODEX Programme of the European Space Agency (ESA) under contract numbers 4000112292, 4000134088, 4000106864, 4000134474, and 4000136424. J.M. acknowledges the financial support from the University start-up grant 3E220031 and the FEDtWIN project PERIHELION. The EUI instrument was built by CSL, IAS, MPS, MSSL/UCL, PMOD/WRC, ROB, LCF/IO with funding from the Belgian Federal Science Policy Office; the Centre National d'Etudes Spatiales (CNES); the UK Space Agency (UKSA); the Bundesministerium für Wirtschaft und Energie (BMWi) through the Deutsches Zentrum für Luft- und Raumfahrt (DLR); and the Swiss Space Office (SSO). The EUI data used here belongs to the EUI data-release 6 (Kraaikamp et al. 2023). The authors thank all the teams responsible for the space-based observations. The data are publicly available at `https://spdf.gsfc.nasa.gov/` (SDO, STEREO) and `https://soar.esac.esa.int/soar/` (SOLO). The authors would also like to thank JHelioviewer for being able to browse LASCO, SECCHI, EUI, AIA, EUVI, and HMI data (`http://jhelioviewer.org`; Müller et al. 2017).

References

Asvestari, E., Pomoell, J., Kilpua, E., et al. 2021, A&A, 652, A27
Bein, B. M., Berkebile-Stoiser, S., Veronig, A. M., Temmer, M., & Vršnak, B. 2012, ApJ, 755, 44
Berger, M. A. 1999, Plasma Phys. Control. Fusion, 41, B167
Berger, M. A. & Ruzmaikin, A. 2000, J. Geophys. Res. (Space Phys.), 105, 10481
Bornmann, P. L., Speich, D., Hirman, J., et al. 1996, in Proc. SPIE, Vol. 2812, GOES-8 and Beyond, ed. E. R. Washwell, 309–319
Brueckner, G. E., Howard, R. A., Koomen, M. J., et al. 1995, Sol. Phys., 162, 357
Chen, J. 2017, Phys. Plasmas, 24, 090501
Chintzoglou, G., Patsourakos, S., & Vourlidas, A. 2015, ApJ, 809, 34
Dissauer, K., Veronig, A. M., Temmer, M., Podladchikova, T., & Vanninathan, K. 2018, ApJ, 863, 169
Domingo, V., Fleck, B., & Poland, A. I. 1995, Sol. Phys., 162, 1
Duan, A., Jiang, C., Zou, P., Feng, X., & Cui, J. 2021, ApJ, 906, 45
Forbes, T. G. 2000, J. Geophys. Res. (Space Phys.), 105, 23153
Gold, T. & Hoyle, F. 1960, MNRAS, 120, 89
Guo, J. H., Ni, Y. W., Qiu, Y., et al. 2021, ApJ, 917, 81
Guo, Y., Schmieder, B., Démoulin, P., et al. 2010, ApJ, 714, 343
Hill, F. 2018, Space Weather, 16, 1488
Hu, Q., Qiu, J., & Krucker, S. 2015, J. Geophys. Res. (Space Phys.), 120, 5266
Inoue, S., Magara, T., Pandey, V. S., et al. 2013, ApJ, 780, 101
Isavnin, A. 2016, ApJ, 833, 267
James, A. W., Green, L. M., Palmerio, E., et al. 2017, Sol. Phys., 292, 71
Kaiser, M. L., Kucera, T. A., Davila, J. M., et al. 2008, Space Sci. Rev., 136, 5
Kraaikamp, E., Gissot, S., Stegen, K., et al. 2023, SolO/EUI Data Release 6.0 2023-01, https://doi.org/10.24414/z818-4163, published by Royal Observatory of Belgium (ROB)
Lemen, J. R., Title, A. M., Akin, D. J., et al. 2012, Sol. Phys., 275, 17
Liu, W., Berger, T. E., Title, A. M., & Tarbell, T. D. 2009, ApJ, 707, L37
Maharana, A., Isavnin, A., Scolini, C., et al. 2022, Adv. Space Res., 70, 1641
Marubashi, K., Akiyama, S., Yashiro, S., et al. 2015, Sol. Phys., 290, 1371
Moffatt, H. K. 1978, Magnetic field generation in electrically conducting fluids (Cambridge, England, Cambridge University Press, 1978. 353 p.)
Müller, D., Nicula, B., Felix, S., et al. 2017, A&A, 606, A10
Murray, M. J. & Hood, A. W. 2008, A&A, 479, 567
Müller, D., St. Cyr, O. C., Zouganelis, I., et al. 2020, A&A, 642
Palmerio, E., Kilpua, E. K. J., James, A. W., et al. 2017, Sol. Phys., 292, 39
Pesnell, W. D., Thompson, B. J., & Chamberlin, P. C. 2012, The Solar Dynamics Observatory (SDO) (New York, NY: Springer US), 3–15
Pomoell, J. & Poedts, S. 2018, J. Space Weather Space Clim., 8, A35
Priest, E. R. & Longcope, D. W. 2017, Sol. Phys., 292, 25
Priest, E. R., Longcope, D. W., & Janvier, M. 2016, Sol. Phys., 291, 2017
Rochus, P., Auchère, F., Berghmans, D., et al. 2020, A&A, 642, A8
Rodriguez, L., Shukhobodskaia, D., Niemela, A., et al. 2024, A&A, 689, A187
Russell, C. T. 1999, Aust. J. Phys., 52, 733
Salas-Matamoros, C. & Klein, K. L. 2015, Sol. Phys., 290, 1337
Scherrer, P. H., Schou, J., Bush, R. I., et al. 2012, Sol. Phys., 275, 207
Scolini, C., Chané, E., Temmer, M., et al. 2020, ApJS, 247, 21
Scolini, C., Rodriguez, L., Mierla, M., Pomoell, J., & Poedts, S. 2019, A&A, 626, A122
Seehafer, N. 1990, Sol. Phys., 125, 219
Temmer, M. 2021, Living Rev. Sol. Phys., 18, 4
Thernisien, A. 2011, ApJS, 194, 33
Titov, V. S. & Démoulin, P. 1999, A&A, 351, 707
Titov, V. S., Downs, C., Mikić, Z., et al. 2018, ApJ, 852, L21
Titov, V. S., Török, T., Mikic, Z., & Linker, J. A. 2014, ApJ, 790, 163
Valentino, A. & Magdalenic, J. 2024, A&A, 690, A137
van Ballegooijen, A., DeLuca, E., Squires, K., & Mackay, D. 2007, J. Atmos. Sol.-Terr. Phys., 69, 24, challenges to Modeling the Sun-Earth System, a Workshop
Verbeke, C., Pomoell, J., & Poedts, S. 2019, A&A, 627, A111
Vourlidas, A., Plunkett, S., Korendyke, C., et al. 2004, in AGU Fall Meeting Abstracts, Vol. 2004, SH21B–0409
Wiegelmann, T. 2004, Sol. Phys., 219, 87–108
Wuelser, J.-P., Lemen, J. R., Tarbell, T. D., et al. 2004, in Society of Photo-Optical Instrumentation Engineers (SPIE) Conference Series, Vol. 5171, Telescopes and Instrumentation for Solar Astrophysics, ed. S. Fineschi & M. A. Gummin, 111–122
Xie, H., Ofman, L., & Lawrence, G. 2004, J. Geophys. Res. Space Phys., 109, A03109
Yan, X. L., Xue, Z. K., Liu, J. H., Kong, D. F., & Xu, C. L. 2014, ApJ, 797, 52

Appendix A: Table

Table A.1: List of the 43 MFRs events used for the study.

1	2	3	4	5	6	7	8	9	10	11	12	13
No.	**Date** mm/dd	**Time** UT	**Obs.**	τ Turns	**Lon** deg	$\tau_{\mathbf{d}}$ Turns	**L** Mm	**a** Mm	$\mathbf{V_{CME}}$ km/s	**Flare**	$\mathbf{AR_a}$	$\mathbf{AR_b}$
	2012											
E1*	07/12	16:10	A	1.9±0.08	0	1.9	141	18	1335	X2.03	11520	$\beta\gamma$
	2014											
E2*	09/10	17:18	A	1.8±0.05	5	1.9	115	15	1122	X2.38	12158	$\beta\gamma\delta$
	2020											
E3	12/07	14:33	A	1.9±0.13	8	2.0	58	5	1179	C7.41	12790	α
		14:32	B1	1.1±0.03	66		48	10				
	2021											
E4*	10/28	15:24	A	2.8±0.15	0	2.8	120	11	1078	X1.00	12887	$\beta\gamma$
		15:23	B1	2.4±0.06	42		106	11				
	2022											
E5	01/16	19:10	A	1.4±0.06	29	2.2	86	14	667	C2.65	12929	β
		19:10	B1	1.6±0.12	63		49	11				
		19:10	C	1.9±0.21	45		82	15				
E6	01/17	13:40	A	1.8±0.08	37	2.5	107	15	475	C2.70	12930	β
		13:40	B2	1.1±0.05	70		65	13				
		13:40	C	1.5±0.08	53		109	17				
E7	01/29	20:50	A	2.2±0.11	0	2.2	61	7	671	M1.10	12936	$\beta\gamma\delta$
		20:50	B1	1.6±0.12	28		56	8				
		20:52	C	1.9±0.21	12		62	9				
E8	02/06	12:04	A	2.2±0.12	0	2.3	254	28	650	C3.10	12939	β
		12:02	B2	1.8±0.04	32		235	31				
		12:02	C	1.9±0.07	17		263	33				
E9	03/10	18:00	A	1.7±0.04	12	2.1	204	29	1168	C2.71	12962	α
		18:00	B1	1.6±0.06	44		183	29				
		18:00	C	1.9±0.15	0		108	27				
E10*	03/28	11:09	A	2.1±0.05	5	2.3	88	10	648	M4.00	12975	$\beta\gamma$
		11:09	B1	1.6±0.09	38		71	11				
		11:10	C	0.8±0.08	76		71	13				
E11*	03/28	18:48	A	1.8±0.04	9	2.2	57	7	836	M1.00	12975	$\beta\gamma$
		18:45	B2	1.4±0.04	44		53	9				
E12	05/25	17:40	A	1.6±0.07	33	2.3	181	27	1051	M1.30	13016	α
E13*	06/13	02:30	A	1.5±0.06	49	2.3	98	16	1016	M3.43	13032	$\beta\gamma$
		02:29	B2	1.62±0.09	25		119	18				
E14*	08/14	11:35	A	2.0±0.12	15	2.4	235	19	810	C2.40	13076	β
		11:35	B1	1.7±0.07	37		213	30				
E15*	08/16	00:55	A	2.3±0.09	6	2.5	115	14	769	C5.90	13078	$\beta\gamma\delta$
		00:55	B2	2.0±0.14	28		110	14				
E16*	08/16	13:21	A	1.9±0.10	15	2.2	71	9	667	C6.40	13078	$\beta\gamma\delta$
		13:22	B2	1.5±0.04	36		60	10				
E17*	08/17	02:05	A	1.3±0.17	38	1.9	45	9	911	M8.77	13110	β
		02:05	B2	0.7±0.07	55		35	11				
	2022											
E18*	10/02	02:05	A	1.3±0.17	38	1.9	45	9	911	M8.77	13110	β
		02:05	B2	0.7±0.07	55		35	11				
E19*	10/02	20:06	A	1.3±0.04	46	2.2	72	13	1249	X1.06	13110	β
		20:05	B2	0.8±0.05	63		57	15				
E20*	12/24	00:09	A	1.6±0.08	30	2.2	214	30	1094	C1.41	13174	β
		00:09	B1	1.8±0.04	17		219	29				
	2023											
E21	01/03	13:22	A	1.5±0.07	29	2.2	98	15	882	C3.40	13176	β
		13:22	B2	1.3±0.03	43		84	15				
E22	02/24	19:49	A	2.0±0.07	27	2.5	258	29	1413	M3.70	13229	β
		19:49	B1	1.8±0.05	41		258	31				
E23	02/25	18:40	A	1.7±0.04	39	2.5	231	30	1112	M6.35	13229	β
		18:40	B1	1.6±0.10	50		176	27				
E24	03/06	02:00	A	1.0±0.05	62	2.3	36	8	813	M5.80	13243	β
		02:00	B1	0.9±0.03	74		30	7				
E25	03/20	13:30	A	2.0±0.09	20	2.1	266	33	965	C4.40	13243	β
		13:30	B1	2.0±0.05	8		282	34				

Table A.1: continued.

1	2	3	4	5	6	7	8	9	10	11	12	13
No.	**Date** mm/dd	**Time** UT	**Obs.**	τ Turns	**Lon** deg	$\tau_{\mathbf{d}}$ Turns	**L** Mm	**a** Mm	$\mathbf{V_{CME}}$ km/s	**Flare**	$\mathbf{AR_a}$	$\mathbf{AR_b}$
		13:30	C	1.8±0.07	1		282	38				
E26	10/16	10:31	A	1.2±0.09	49	2.1	94	19	787	C7.40	13267	α
		10:30	B2	1.1±0.12	53		100	21				
		10:31	C	1.9±0.12	7		142	18				
E27	11/27	18:14	A	2.2±0.09	15	2.4	129	15	491	C	-	-
		18:15	B2	2.0±0.09	21		200	24				
		18:13	C	2.2±0.06	5		198	22				
E28	11/27	23:00	A	2.2±0.15	19	2.4	583	66	1085	C5.50	13503	α
		23:00	B2	2.1±0.12	25		592	68				
		23:00	C	2.0±0.10	9		651	82				
E29*	11/28	19:13	A	2.0±0.17	0	1.9	118	15	791	M9.82	13500	$\beta\gamma$
		19:13	B1	1.8±0.17	5		122	17				
		19:13	C	1.5±0.21	12		125	19				
	2024											
E30*	01/02	18:11	A	1.9±0.15	52	2.8	81	11	510	M1.15	13536	$\beta\gamma$
		18:12	B2	1.6±0.07	60		80	12				
		18:11	C	2.1±0.16	36		87	10				
E31	01/09	20:09	A	1.7±0.10	72	3.0	102	15	717	-	-	-
		20:09	B1	1.4±0.07	82		128	22				
		20:11	C	1.9±0.12	53		118	16				
E32	01/22	08:50	A	3.0±0.14	2	3.0	524	44	957	-	-	-
		08:50	B1	2.8±0.17	5		568	52				
		08:50	C	2.6±0.14	27		462	45				
E33	03/10	22:25	A	1.7±0.14	25	2.3	92	13	744	C1.20	13603	α
		22:25	B2	1.8±0.05	16		112	15				
		22:25	C	1.5±0.03	42		96	15				
E34*	03/25	12:31	A	1.5±0.06	50	2.6	115	19	544	C2.00	13622	β
		12:32	B2	1.4±0.11	58		111	19				
		12:31	C	1.3±0.14	68		85	16				
E35	05/09	17:11	A	2.3±0.10	26	2.5	86	9	1057	X1.10	13664	$\beta\gamma\delta$
		17:13	B1	1.9±0.15	14		91	12				
E36	05/10	06:09	A	1.9±0.06	33	2.6	90	11	1031	X4.00	13664	$\beta\gamma\delta$
		06:09	B1	2.2±0.11	21		118	13				
	2024											
E37	10/09	01:31	A	2.6±0.04	10	2.9	176	17	1168	X1.84	13848	$\beta\gamma\delta$
		01:30	B1	2.3±0.17	14		165	18				
		01:31	C	2.1±0.12	65		140	16				
E38	10/11	15:41	A	2.3±0.18	25	2.8	79	9	438	M2.14	13854	$\beta\gamma$
		15:40	B1	1.8±0.05	50		67	9				
		15:40	C	2.3±0.25	19		90	10				
E39*	10/30	09:02	A	2.6±0.29	18	2.9	242	24	-	C7.10	13876	$\beta\gamma$
		09:03	B1	2.7±0.03	11		260	24				
		09:01	C	2.2±0.11	29		235	27				
	2025											
E40	01/22	10:37	A	2.3±0.13	11	2.4	135	14	572	M1.35	13961	$\beta\gamma$
		10:38	B1	2.0±0.14	17		139	17				
		10:37	C	1.6±0.14	30		138	21				
E41*	01/31	13:43	A	2.3±0.31	46	3.3	179	20	377	M6.76	13978	$\beta\gamma$
		13:43	B1	2.1±0.24	76		187	33				
		13:43	C	2.5±0.23	25		216	22				
E42	03/17	18:40	A	1.4±0.06	50	2.5	104	18	542	M1.00	14033	α
		18:40	B1	1.2±0.06	76		123	24				
		18:41	C	1.2±0.08	60		103	20				
E43*	03/21	15:30	A	2.5±0.31	29	2.9	167	16	424	M1.22	14028	β
		15:30	B1	2.9±0.24	0		184	1				
		15:30	C	2.5±0.23	6		176	15				
[2]												

[2] Column 1: Event number, (*) indicates higher complexity in defining the PIL. Column 2 & 3: Date and time of the measurement, respectively. Column 4: Instrument and wavelength used to measure the twist, where A = AIA 171 Å, B1 (B2) = EUVI 171 (195) Å, and C = EUI 174 Å. Column 5: Absolute averaged twist measured per event and instrument and standard error. Column 6: Absolute longitude relative to the instrument viewpoint. Column 7: Average twist per event, de-projected to the central meridian. Column 8 & 9: Averaged flux rope length and width, respectively, measured per instrument. Column 10: CME speed estimated from coronagraph 3D CME-reconstruction. Column 11: Associated flare number. Column 12: NOAA AR number. Column 13: Hale classification of the AR.

Appendix B: Tool guidelines

We developed an interactive tool in Python environment to estimate the twist of MFR using the proposed method. This appendix provides details about its functionality and a guide for its usage.

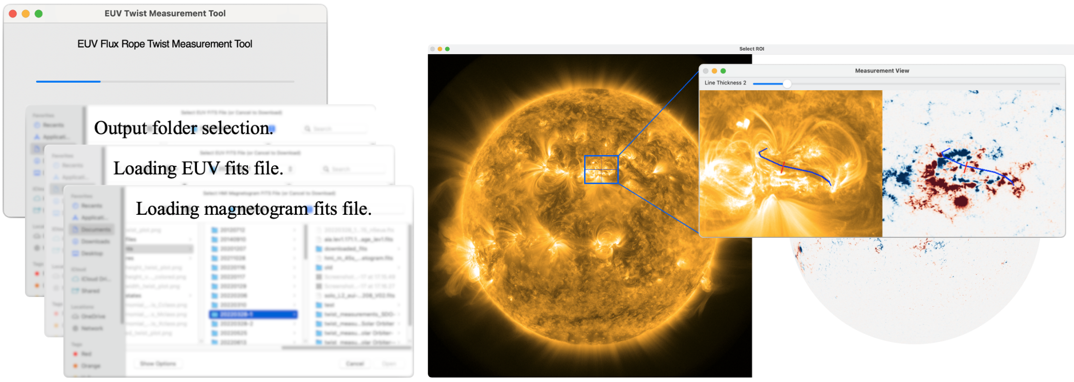

(a) (b)

Fig. B.1: Illustrative example of the interactive interface. (a) Selection of the local output folder. The needed fits files are obtained from the selected folder. The tool can also automatically download the fits files if needed. (b) The area of interest is selected ("Select ROI"). Lastly, the ratio is measured and the twist calculated.

1. Input data
   The tool employs a selected EUV image and the closest in time magnetogram in FITS (Flexible Image Transport System) format. At the start the tool requests the source folder of the FITS files. This step should be skipped when the FITS files are automatically downloaded after specifying the instrument (e.g., SDO/AIA, STEREO/EUVI, SolO/EUI), wavelength, and timestamp.
2. Image loading and selection of area
   The EUV and magnetogram images are displayed side by side. The user then defines a region of interest (ROI) by drawing a square on top of the EUV image.
3. Measurements
   An interactive window opens allowing the user to trace:
   – The flux rope axis (blue lines), determined by EUV morphology and guided by the magnetogram to locate footpoints L.
   – The flux rope width (red line), representing its cross-sectional diameter a.
   The tool detects the blue and red lines as MFR axis and width, respectively, and it is not interchangeable unless the code is modified. The user can perform several measurements before the session is closed. The tool saves the information of each measurement. A measurement can be redone before closing the tool it and moving on the the next measurement. Although the magnetogram can help in identification of the footpoints, the precise selection of the measured quantities still strongly depends on the experience of the user.
4. Twist calculation and error estimation
   Upon completion of measurements the tool computes the aspect ratio L/a and applies Eq 1 to calculate τ. It also quantifies the standard error and average value of the twist.
5. Data storage and reproducibility
   The values of L, a, and τ for each measurement as well as the average values and standard errors are recorded in a text file. The tool also saves pixel coordinates for reproducibility and the cropped EUV and magnetogram image resulted from each measurement in .png format.

The tool features an intuitive, user-friendly interface and delivers results efficiently and fast. This ensures that the method can be seamlessly integrated into space weather forecasting pipelines, facilitating rapid twist estimation as part of real-time CME analysis workflows. The latest version of the tool code can be found in `https://doi.org/10.5281/zenodo.15864359`.